

# Copper-driven catalyst design for improved oxygen reduction reactions in carbon-based materials

Arseniy Kalnin, Ksenia Kharisova, Daniil Lukyanov, Oleg Levin and Elena Alekseeva\*

Institute of Chemistry, St. Petersburg University, Universitetskaya emb, Saint Petersburg, 7/9, 199034, Russian Federation.

## ABSTRACT

The oxygen reduction reaction (ORR) plays a critical role in various energy conversion and storage platforms, making it imperative to develop catalysts which are not only highly efficient, but also economically viable. Carbonaceous materials doped with non-noble metals, especially copper, have emerged as a promising alternative to precious metal catalysts. Despite serious efforts in this direction, the meticulous adjustment of the catalytic efficacy of these materials remains a challenging task. Given this pressing need, we propose a multifaceted strategy for the systematic design of catalytically active agents based on a copper complex anchored in a ligand containing a pyridine form of nitrogen. This intricate complex serves a dual purpose: it orchestrates the environment of copper atoms by embedding them amidst nitrogen moieties, thereby preventing their propensity to agglomerate. At the same time, it fulfills the role of a nitrogen source, directing the onset of structural defects. In particular, the dimensions of the metal clusters within these catalysts are significantly reduced compared to their conventional counterparts. This feature results in an improvement of their electrochemical properties and enhances the kinetics governing the ORR process.

**KEYWORDS:** oxygen reduction reaction, cobalt-doped carbons, catalytic performance, nitrogen-rich environment, methanol tolerance.

## 1. INTRODUCTION

The electrocatalytic oxygen reduction reaction (ORR) is of paramount importance for the optimal functioning of fuel cells and zinc-air batteries. As a result, it has attracted considerable scientific interest and scrutiny [1]. The use of platinum-catalyzed carbon electrodes has become the dominant technology in commercial alkaline fuel cells and zinc-air batteries [2]. These carbon electrodes are economical and durable, ensuring stability over time.

Unfortunately, they suffer from sluggish oxygen adsorption and oxygen reduction reaction (ORR) activity. Consequently, an abundance of active material is required, which has a negative impact on the mass and volumetric power densities of fuel cells and batteries. By contrast, noble metal-free catalysts, especially platinum-free, exhibit much higher ORR efficiency at the cost of increased cost and vulnerability to catalyst toxicity and aging [3]. Therefore, developing efficient and economically viable noble metal-free catalysts capable of enhancing ORR activity becomes imperative to raise the performance thresholds of fuel cells and Zn-Air batteries. In addition, a noble metal-free catalyst would offer striking advantages in terms of reduced cost and improved durability, even if equipped with equivalent catalytic activity.

A variety of noble metal-free catalysts for the oxygen reduction reaction (ORR) have been extensively studied in the scientific literature [4]. In particular, molecular [5-7] and macromolecular [8-10] coordination compounds with transition

---

\*Corresponding author: e.v.alekseeva@spbu.ru

metals such as iron (Fe), cobalt (Co), and copper (Cu) have emerged as highly effective ORR catalysts. Substantial advances have been made in enhancing the oxygen adsorption and catalytic ORR activity of carbonaceous materials through the selective introduction of nitrogen and sulfur [11, 12].

In addition, the efficacy of nitrogen-doped carbon (CN) materials as ORR catalysts can be further enhanced by incorporating metallic constituents into the material. Such doping can occur both as single atom dopants and as metal arrays interacting within the carbon matrix. In the first case, the coordination environment of the metal atom closely matches that of coordination compounds, thereby inducing similar ORR behavior [13]. Nitrogen doping is recognized as an effective method to increase the ORR activity of CN. The use of nitrogen-rich precursors could increase the nitrogen content of CN. Polyacrylonitrile (PAN) polymer stands out as an exemplary precursor due to its nitrogen-rich composition. PAN effectively coordinates transition metal ions *via* its -CN groups [14, 15].

In this study, we propose the use of copper complexes with 1-(2-pyridylazo)-2-naphthol as the metal source for the preparation of ORR catalysts using a two-step carbonization process involving the impregnation of PAN with these complexes [16]. Pyridinic nitrogen in 1-(2-pyridylazo)-2-naphthol provides direct coordination to copper centers, making it advantageous for carbonization. In addition, the organic milieu of the complex enhances its solubility within the PAN matrix, potentially promoting a more homogeneous dispersion of metal atoms. Our investigation shows that copper catalysts prepared with cobalt 1-(2-pyridylazo)-2-naphthol (L) complexes exhibit enhanced catalytic activity compared to those prepared with cobalt acetate. The smaller size and more uniform distribution of metal particles derived from the complex metal source may explain this difference.

## 2. MATERIALS AND METHODS

### 2.1. Materials

Commercially available PAN with a molecular weight (Mw) of 150 kDa was procured from local

suppliers. Cobalt acetate tetrahydrate ( $\text{Cu}(\text{OAc})_2 \cdot 4\text{H}_2\text{O}$ ) and 1-(2-pyridylazo)-2-naphthol were obtained from reliable sources. The cobalt complex of 1-(2-pyridylazo)-2-naphthol, denoted as  $\text{CuL}_2$ , was synthesized following established protocols in the scientific literature [17].

### 2.2. Synthesis of the catalysts

A solution comprising 2 mg of PAN dissolved in 2.2 ml of N,N-dimethylformamide (DMF) was mixed with 0.35 mmol of the respective cobalt precursor. The resultant solution was then added to a mixture consisting of 20 ml of isopropanol (iPrOH) and 2 ml of glycerol pre-heated to 50 °C. The mixture was homogenized for a duration of 20 minutes. The resulting dispersion was sealed within a 150 ml stainless steel pressure reactor equipped with a PTFE gasket and subjected to heating at 180 °C for 6 hours. Following the heating step, the precipitate generated from the reaction mixture was collected *via* centrifugation, subjected to thorough washing with iPrOH, and subsequently dried at 80 °C for 6 hours in an oven. This was followed by an additional 12 hours of drying under vacuum conditions at 80 °C. The pretreated sample was then subjected to controlled heating in a tube furnace equipped with a quartz tube for a duration of 2 hours. The heating process was carried out in an argon atmosphere with a purity level of 99.995%. After heating, the sample was gradually cooled under argon and subsequently manually ground using a mortar.

### 2.3. Characterization techniques

The morphological features and particle size of the catalysts were evaluated through microphotography employing an AURIGA CrossBeam scanning electron microscope (Carl Zeiss Group). Surface area and porosity assessments were conducted by analyzing nitrogen adsorption-desorption isotherms using a Nova Series 1200e analyzer (Quantachrome Instruments), with data processed *via* the BET and BJH methods. X-ray diffraction (XRD) spectra were recorded using an AXS D8 DISCOVER diffractometer (Bruker) with a  $\text{CuK}\alpha$  source ( $\lambda = 1.5418 \text{ \AA}$ ) in the angular range of 15-90°. The average interlayer spacing between aromatic layers (d002) was determined using Bragg's equation. Cobalt crystallite size (DCo) was computed utilizing the Scherrer formula:

$DCo=0.9\lambda/B111\cos(\phi111)$ , where  $\lambda$  represents the X-ray wavelength,  $B$  and  $\phi$  denote the full width at half maximum (FWHM) and the corresponding scattering angle of the diffraction peak, respectively.

Raman spectra were acquired utilizing a Senterra spectrometer (Bruker) equipped with a 20 mW 488 nm laser. Fourier-transform infrared (FT-IR) spectra were recorded using a Vertex 70 infrared spectrometer (Bruker) across the wave number range of 500-3700  $\text{cm}^{-1}$  with a spectral resolution of 2  $\text{cm}^{-1}$ .

X-ray photoelectron spectroscopy (XPS) measurements were conducted employing a Thermo Fisher Scientific Escalab 250Xi photoelectron spectrometer, employing  $AlK\alpha$  radiation with a photon energy of 1486.6 eV. Spectra were recorded in the constant pass energy mode at 50 eV for element core level spectrum and 100 eV for survey, utilizing a 650  $\mu\text{m}$  spot size with a total energy of 0.2 eV. To neutralize surface charge resulting from emitted photoelectrons, a dual-mode charge compensation mechanism comprising low-energy electrons and argon was employed. The investigations were conducted at room temperature within an ultrahigh vacuum environment of approximately  $10^{-9}$  mbar. Peaks in the spectra were fitted using a product of asymmetric Gaussian and Lorentzian line shapes.

#### 2.4. Electrochemical analysis

Electrochemical data was recorded using a BioLogic VMP3 potentiostat and Autolab rotating disk electrode (RDE) device. Measurements were carried out within a three-electrode cell configuration employing a glassy carbon (GC) electrode with a surface area of 0.07  $\text{cm}^2$  as the working electrode. A saturated AgCl/KCl electrode served as the reference electrode, while a platinum (Pt) wire acted as the counter electrode. The electrolyte, a 0.1 M KOH/ $\text{H}_2\text{O}$  solution, underwent purging with argon (Ar) or oxygen ( $\text{O}_2$ ) for a duration of 10 minutes prior to experimentation and was maintained under a continuous gas flow during measurements. In RDE experiments, uninterrupted  $\text{O}_2$  purging through the electrolyte was maintained to sustain saturated gas concentration.

The potential of the working electrode was cycled between +0.3 V and -0.9 V vs. the reference electrode at a scan rate of 10  $\text{mV s}^{-1}$ . The presented data were adjusted to the reversible hydrogen electrode (RHE) by adding 0.978 V. The ORR activity of the investigated materials was assessed using the rotating disk electrode (RDE) method, with varying RDE rotation speeds of 500, 1000, 2000, 3000, 4000, and 5000 rpm.

### 3. RESULTS AND DISCUSSION

#### 3.1. Catalyst preparation

The synthesis of copper-doped CN catalysts was executed in a three-step process. At the first step, PAN was impregnated with the chosen cobalt precursor *via* co-precipitation from a DMF solution. Subsequently, solvothermal treatment of the Cu-impregnated PAN in isopropanol (iPrOH) followed. Lastly, high-temperature carbonization was conducted in an argon (Ar) flow. Two distinct cobalt precursors were employed:  $\text{Cu}(\text{OAc})_2 \cdot 4\text{H}_2\text{O}$ , offering DMF-soluble, weakly coordinated  $\text{Cu}^{2+}$  ions, and the cobalt complex  $\text{CoL}_2$ , known for providing strongly coordinated  $\text{Cu}^{2+}$  ions involving pyridine-containing ligands. Catalysts were labeled in accordance with the cobalt precursor used and the carbonization temperature 700  $^\circ\text{C}$ , as detailed in Table 1.

#### 3.2. Catalyst characterization

As shown in Figure 1, the characterization of the catalysts provided interesting insights. Distinctive structural features can be seen in the scanning electron microscopy (SEM) images of the samples. The surface of CuAcCN is full of agglomerated metallic nanoparticles with an average size in the range of 100-200 nm (Figure 1a). A morphology with a pronounced amorphous

**Table 1.** Labels, Cu precursors and carbonization temperatures of prepared catalysts.

| Label                   | Cu precursor  |
|-------------------------|---|
| CN                      | -   |
| CuAcCN                  | $\text{Cu}(\text{OAc})_2 \cdot 4\text{H}_2\text{O}$ |
| $\text{CuL}_2\text{CN}$ | $\text{CuL}_2$                                      |

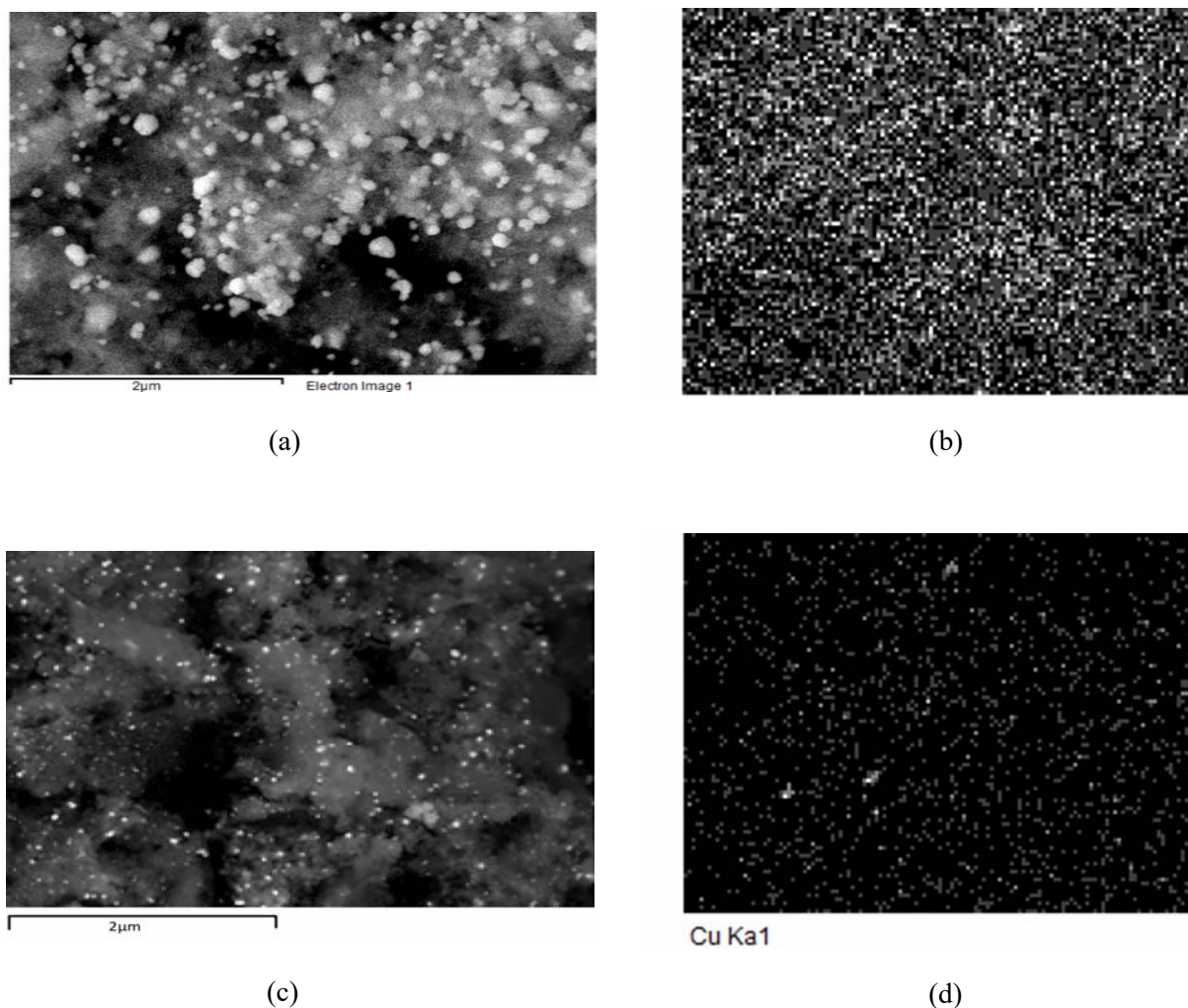


**Figure 1.** SEM images of the catalysts (a) CuAcCN; (c) CuL<sub>2</sub>CN; EDX images of the catalysts (b) CuAcCNx; (d) CuL<sub>2</sub>CNx.

fraction is observed in the CoL<sub>2</sub>CN sample. In this sample, the size of the active metal particles can be reduced several times by using 1-copper (2-pyridylazo)-2-naphthol as a copper source (Figure 1b). The comparison of the results of the EDX analysis confirms the conclusions drawn from the SEM images. By comparing Figures 1b and c, it can be concluded that the use of the ligand leads to a uniform distribution of Cu nanoparticles in the catalyst.

To study the defects in the catalyst structure, Raman spectroscopy was performed. Peak positions of each sample were almost identical at about 1340 and 1600 cm<sup>-1</sup>, corresponding to D and G bands, respectively. The ratio of the

intensities of the ID/IG bands in their Raman spectra was used to determine the degree of disorder of the catalysts obtained. The higher the ratio, the more defects and the less ordered the structure. The CN catalyst showed the highest relationship among all samples. This shows that the carbon structure is influenced by both the pyrolytic temperature and the copper source.

To confirm the structural changes in the samples, Fourier Transform Infrared spectroscopy (FTIR) was performed to identify characteristic vibrations. The FTIR spectra (Figure 2b) of all the samples showed transmission bands due to the vibrations of C-N, C=N, C=C, and C-C.

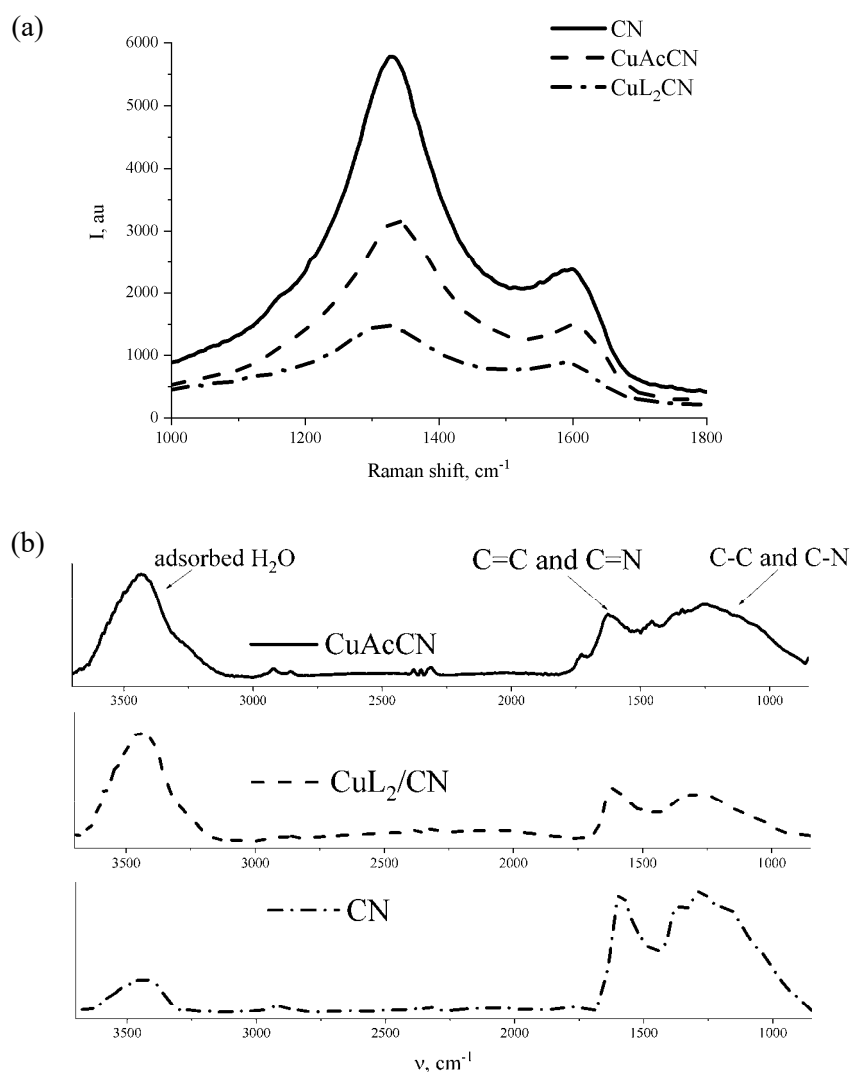


**Figure 2.** (a) Raman spectra and (b) FTIR of the CuAcCN and CuL<sub>2</sub>CN catalysts.

The bands at 1614 and 1260  $\text{cm}^{-1}$  are indicative of the C=N and C-N vibrations, respectively, which correspond to the disordered carbon. The samples also showed bands at 3127  $\text{cm}^{-1}$ , which are correspondingly assigned to the O-H vibrations of the water that is adsorbed on the surface.

X-ray photoelectron spectroscopy (XPS) analysis was used to determine the elemental composition and the chemical state of the atoms in the materials.

High resolution N<sub>1s</sub> XPS spectra were deconvoluted into four nitrogen species: pyridine N (398.3eV), pyrrole N (400.2eV), graphite N (401.2eV), and oxidized N (402.1eV) (Figure 3)

[18]. The nitrogen peaks in the XPS spectra for the CuAcCN and CuL<sub>2</sub>CN catalysts have the same binding energies, indicating that pyridinic N and graphitic N are the predominant catalytically active sites for anchoring and stabilizing Cu atoms [19]. Depending on the composition of the catalysts, the intensity ratio of the peaks is different. The pyridinic nitrogen peak is more intense than the pyrrolic and graphitic nitrogen peaks for the CuL<sub>2</sub>CN catalyst. This indicates that the nitrogen on the surface of these catalysts is predominantly in the pyridinic state, which is likely to contribute to the higher activity of the CuL<sub>2</sub>CN catalyst as compared to the CuAcCN catalyst.

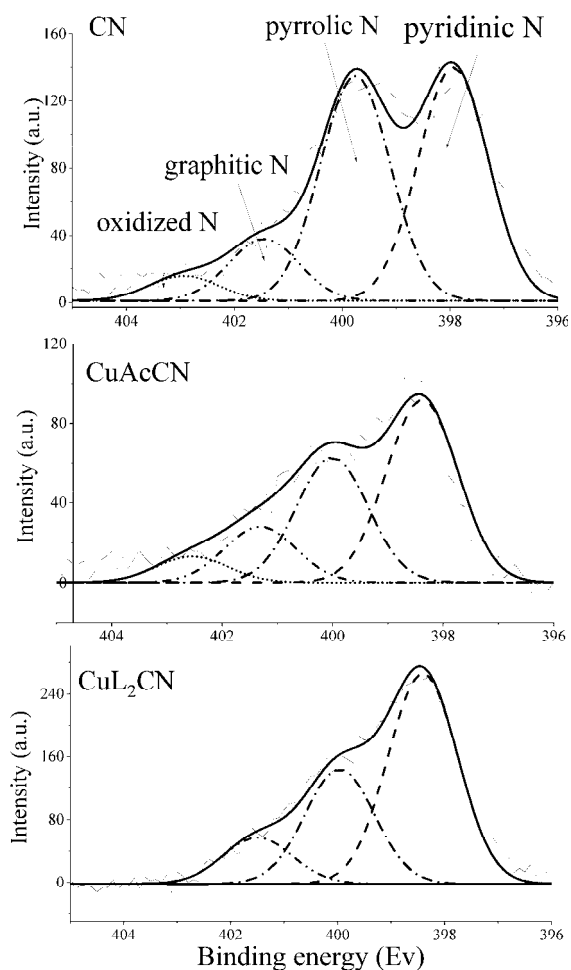


**Figure 3.**  $N_{1s}$  XPS spectra of the catalysts.

### 3.3. Electrocatalytic properties

To investigate the ORR kinetics, the RDE method was utilized, and the corresponding voltammograms recorded at 5000 rpm are presented in Figure 4a. The CN catalyst has the lowest reduction current under these conditions. Accordingly, the limit current of  $CoL_2CN$  is higher than  $1.4 \text{ mA cm}^{-2}$  and  $3.7 \text{ mA cm}^{-2}$  for CuAcCN and CN catalysts. The ORR currents for this particular material at different rotation rates are shown in Figure 4b.

The difference in the number of electrons involved in the ORR is responsible for the difference in the diffusion currents between the  $CoL_2CN$  and the Pt/C. The Levich-Koutecky (LK) method (Figure 5) was used to estimate the number of electrons.

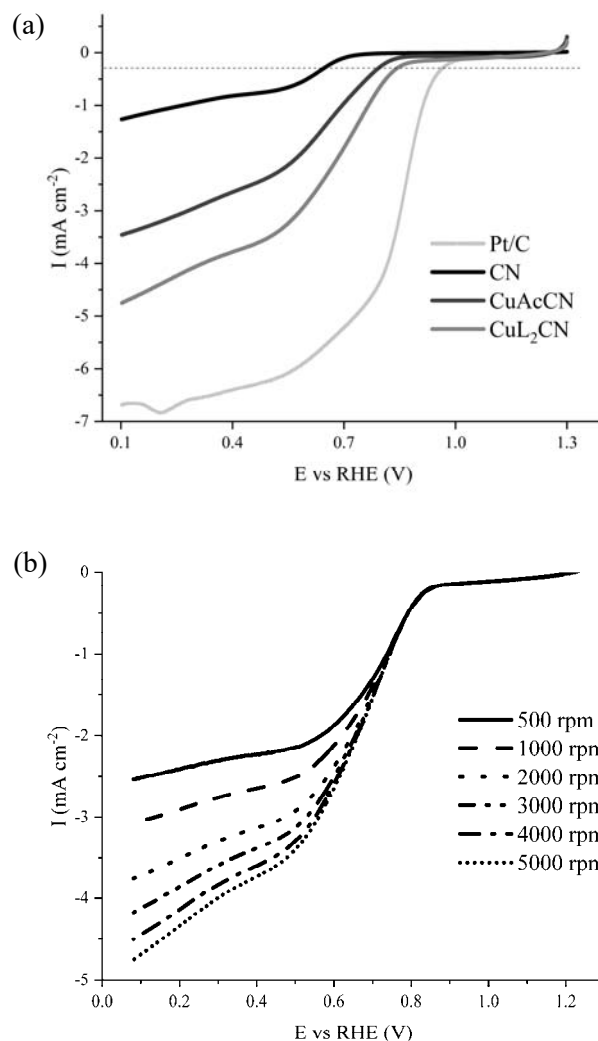


**Figure 4.** (a) RDE voltammograms of investigated materials in 1M KOH electrolyte purged with  $O_2$  measured at 5000 rpm, (b) RDE cyclic voltammetry of  $CoL_2CN_{x-1100}$  in 1M KOH electrolyte purged with  $O_2$ .

For both Cu- and Pt/C-based catalysts, slopes are close to a four-electron mechanism of ORR. From the data obtained, it can be concluded that the oxygen reduction reaction proceeds efficiently on the copper catalysts obtained in this work.

### 4. CONCLUSIONS

In this study, using copper 1-(2-pyridylazo)-2-naphthol complex as metal source, we have applied an active metal source strategy for the synthesis of Cu and N-doped carbon catalysts. The morphology of the obtained CN materials was found to be strongly influenced by the nature

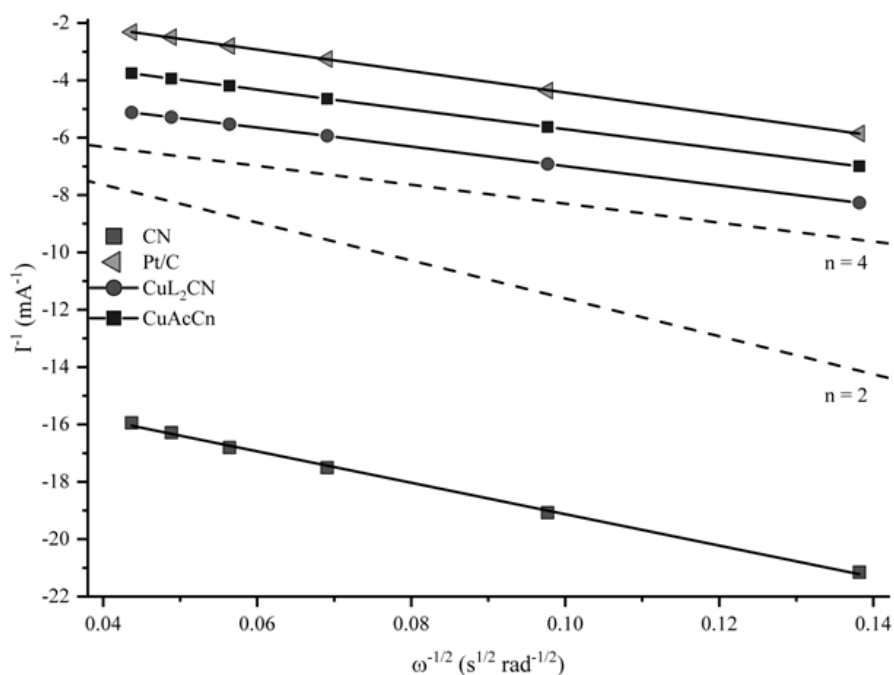


**Figure 5.** Levich-Koutecky analysis of RDE voltammograms of investigated materials in 1M KOH electrolyte purged with  $O_2$ .

of the metal source and the carbonization temperature. SEM, BET, XRD, FPS, and Raman analyses show that  $CuL_2CN_x$  exhibits significantly higher surface area, total pore volume, smaller Cu grain size, and higher pyridinic N content.

The structure and morphology of the resulting materials are also affected by the carbonization temperature of the  $CuL_2$  containing polyacrylonitrile. In summary, the choice of copper precursor affected the morphology, structure and electrochemical properties of the catalysts. The results contribute to a better understanding of the relationship between synthesis parameters and the performance of carbon-based catalysts, and highlight the potential for further optimization and development in electrocatalytic applications.

#### ACKNOWLEDGEMENTS

The research was supported by Russian Science Foundation (project # 22-13-00035). Physicochemical studies were performed at the Interdisciplinary Resource Center in Nanotechnology, Centre for Optical and Laser Materials Research, Centre for X-ray Diffraction Studies, Thermogravimetric and Calorimetric Research Centre and Centre for

Physical Methods of Surface Investigation and Cryogenic Centre (all belonging to Saint Petersburg State University). The article is devoted to the 300<sup>th</sup> anniversary of the founding of St. Petersburg State University.

#### CONFLICT OF INTEREST STATEMENT

The authors declare no conflict of interest

#### REFERENCES

1. Li, Y., Li, Q., Wang, H., Zhang, L., Wilkinson, D. P. and Zhang, J. 2019, *Electrochem. Energy Rev.*, 2, 518-538.
2. Ma, R., Lin, G., Zhou, Y., Liu, Q., Zhang, T., Shan, G., Yang, M. and Wang, J. 2019, *Comput. Mat.*, 5, 78.
3. Debe, M. K. 2012, *Nature*, 486, 43-51.
4. Jaouen, F., Proietti, E., Lefèvre, M., Chenitz, R., Dodelet, J.-P., Wu, G., Chung, H. T., Johnston, C. M. and Zelenay, P. 2011, *Energy Environ. Sci.*, 4, 114-130.
5. Pegis, M. L., Wise, C. F., Martin, D. J. and Mayer, J. M. 2018, *Chem. Rev.*, 118, 2340-2391.

6. Oldacre, A. N., Friedman, A. E. and Cook, T. R. 2017, *J. Am. Chem. Soc.*, 139, 1424-1427.
7. Zhang, R. and Warren, J. J. 2020, *J. Am. Chem. Soc.*, 142, 13426-13434. doi:10.1021/jacs.0c03861.
8. Konev, A. S., Kayumov, M. Y., Karushev, M. P., Novoselova, Y. V., Lukyanov, D. A., Alekseeva, E. V. and Levin, O. V. 2018, *ChemElectroChem*, 5, 3138-3142.
9. Petrov, A. A., Lukyanov, D. A., Kopytko, O. A., Novoselova, J. V., Alekseeva, E. V. and Levin, O. V. 2021, *Catalysts*, 11, 729.
10. Bashyam, R. and Zelenay, P. 2006, *Nature*, 443, 63-66.
11. Wu, Z., Iqbal, Z. and Wang, X. 2015, *Front. Chem. Sci. Eng.*, 9, 280-294.
12. Winston Duo, W., and Dan, X. 2018, *Electrocatalysts for Fuel Cells and Hydrogen Evolution*, R. Abhijit, M. Indrajit and K. P. Ranjan (Ed.), IntechOpen: Rijeka, Ch. 3.
13. Tang, Y., Allen, B. L., Kauffman, D. R. and Star, A. 2009, *J. Am. Chem. Soc.*, 131, 13200-13201.
14. Costa de Oliveira, M. A., D'Epifanio, A., Ohnuki, H. and Mecheri, B. 2020, *Catalysts*, 10, 475.
15. Saha, B. and Schatz, G. C. 2012, *J. Phys. Chem. B*, 116, 4684-4692.
16. Sazanov, Y. N., Fedorova, G. N., Gubanova, G. N. and Sukhanova, T. E. 2014, *Mendeleev Commun.*, 24, 239-241.
17. Mochizuki, K. and Fujimoto, M. 1985, *Bull. Chem. Soc. Jpn.*, 58, 1520.
18. Liu, Z., Wang, M., Luo, X., Li, S., Li, S., Zhou, Q., Xu, W. and Wu, R. 2021, *Appl. Surf. Sci.*, 544, 148912.
19. Akitsu, T. and Einaga, Y. 2007, *Inorg. Chim. Acta*, 360, 497-505.